# Flexible Mm-Wave Sigma-Delta-Over-Fiber MIMO Link

N.B. When citing this work, cite the original published paper.

(article starts on next page)

# Flexible mm-Wave Sigma-Delta-over-Fiber MIMO Link

Husileng Bao, *Student Member, IEEE,* Filippo Ponzini, and Christian Fager, *Senior Member, IEEE*

*Abstract*—Millimeter-wave and multiple-input-multiple-output (MIMO) technologies combine broad bandwidth with spatial diversity to offer a greater data rate. This paper investigates a flexible millimeter-wave sigma-delta-over-fiber based transmitter solution with digital beamforming MISO and MIMO functionality. Those functions are controlled by a central unit connecting a remote radio head with a standardized QSFP28 fiber link. The central unit generates binary encoded intermediate frequency signals using bandpass sigma-delta modulation. The QSFP28 based fiber link transmits the intermediate frequency bitstreams to the remote radio head. The remote radio head consists of a QSFP28 module, 90° hybrids, and upconverters. The remote radio head feeds four parallel, independent, coherent, and central-unit controlled 28 GHz signals to a linear array transmitting antenna. The transmitter performance is experimentally verified, demonstrating up to 800 Msym/s at an EVM/NMSE of 6.7%/-23.5 dB when tested with a 64 quadrature amplitude modulation (64-QAM) modulation scheme. Digital over-the-air beamforming MISO functionality is demonstrated up to 700 Msym/s across 1 m wireless distance. MIMO communication capabilities is demonstrated by over-the-air transmission of two independent 500 Msym/s to two spatially separated receivers. The results show that the proposed link can be used for realization of scalable, low-cost and flexible transmitter solution for emerging distributed antenna systems.

*Index Terms*—MIMO, sigma-delta modulation, mm-Wave, radio-over-fiber, 5G, beamforming.

## I. INTRODUCTION

THE initial 5G networks offer more bandwidth to mobile users by enhanced Mobile Broadband (eMBB) services at the Non-Standalone stage [1]. In its further evolution, 5G will offer Ultra-Reliable Low Latency Communications (URLLC), massive Machine-Type Communications (mMTC) and reach data rates of tens of Gbps [2] [3]. The millimeter-wave (mm-Wave) frequency bands offer greater data throughput than the lower bands [4]. However, mm-Wave signals suffer from weak penetration and high propagation loss [5], limiting the available communication capacity in practice. Multiple-input-multiple-output (MIMO) with beamforming is the most promising solution to compensate propagation loss and at the same time deliver high communication capacity using spatial diversity [6] [7]. To maximize capacity, a combination of mm-Wave transmission and MIMO technology is therefore desired.

Centralized radio access networks (C-RAN) move the majority of computationally intense processing into a central unit (CU), which allows the remote radio heads (RRHs) to be simplified [8]. Radio-over-Fiber (RoF) is a family of techniques of C-RAN, as well as mature technologies for 4G and 5G wireless access networks [9] [10]. As a candidate of C-RAN, this paper studies flexible digital beamforming MISO and MIMO functionalities controlled by a CU and enabled by a simple mm-Wave RRH connected by a standardized fiber link.

In sub-6 GHz frequency bands, RoF is already well established with state-of-the-art analog-radio-over-fiber (ARoF) [11], digital-radio-over-fiver (DRoF) [12] and sigma-delta-over-fiber (SDoF) [13] [14] implementations. The study in [15] states that ARoF enables the simplest RRH and is cost effective for deployment. But [16] [17] criticize that ARoF suffers from nonlinear distortion from the optical components. DRoF has inherently higher tolerance for nonlinearity by transmitting a constant amplitude bitstream [9]. For DRoF, on the other hand, the RRH needs to include complicated real-time signal processing functions and a high-speed digital-analog converter (DAC) which increases the cost [12]. SDoF has a simple radio structure as ARoF, and promises the same linearity advantages as DRoF [16]. SDoF permits to have simpler RRH, compared with DRoF. This becomes more and more important in distributed MIMO implementations, where the number of RRH increases a lot. SDoF has therefore emerged as a practical solution and triggered intense research [13] [14]. However, these low-frequency solutions [11]–[14] can not be easily scaled up to mm-Wave frequencies.

At mm-Wave, several experimental single-input-single-output (SISO) systems based on ARoF have been demonstrated [18]–[22], however implemented with advanced laboratory instruments. The work in [23] is a centrally controlled multiple-input-single-output (MISO) system, but the beam direction is fixed. A simple mm-Wave ARoF is studied in [24], in which the signal is directly generated in the optical domain. However, [24] only supports analog beamforming function. A D-band (110 GHz – 170 GHz) ARoF system reached the highest data rate of 352 Gb/s with a $2 \times 2$ antenna configuration [25]. However, this system [25] depends on a directive narrow beam of horn antennas and does not support MIMO precoding. In [26], another ARoF MIMO system, with Mach-Zehnder Modulator at the CU, is presented. In this way, the RRH recovers mmWave by a photodetector, but the complexity of the CU is high. One of the more mature mm-Wave MIMO systems is reported in [27] and demonstrated during the 2018 PyeongChang Winter Olympics with a 1 GHz bandwidth at
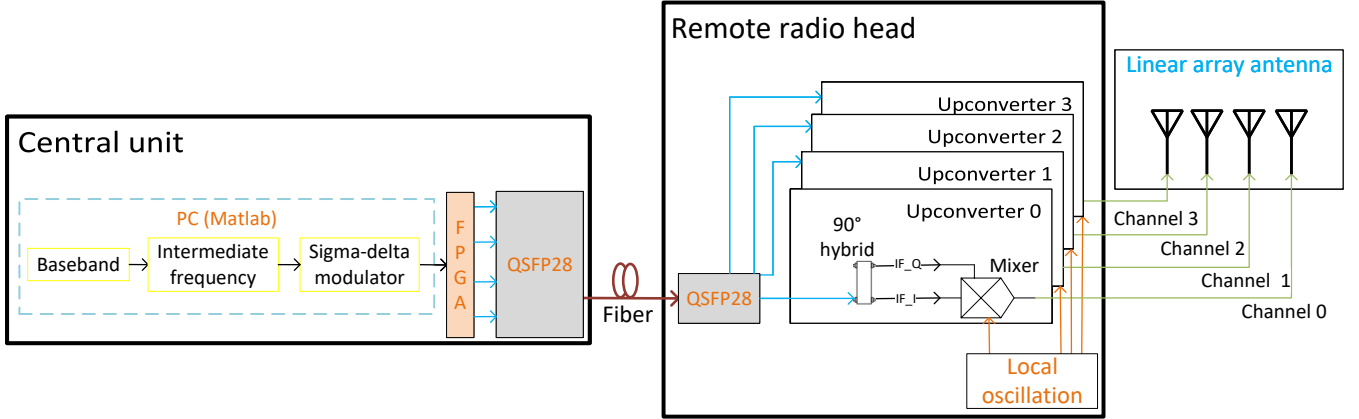
Fig. 1: Proposed link architecture. The QSFP28 connects the central unit and the remote radio head with four independent channels. At the central unit, the PC and FPGA (VCU128) generate the sigma-delta modulated bitstreams to the fiber connection. The remote radio head has four parallel upconversions to radiate signal through a linear array patch antenna.

28 GHz carrier frequency. Since it is a commercial system, it is based on proprietary hardware and signal processing to support commercial requirements. Such high cost and great efforts of RRH design in [27] reduces the possibility for scientific MIMO research. In [28], an SDoF solution with real-time sigma-delta-modulation (SDM) is demonstrated for 22.75 GHz – 27.5 GHz carrier frequency range. However, the achieved symbol rate is limited to 390 Msym/s performance from an excessive 100 Gbps bitrate. Recently, another SDoF-based digital RoF system was proposed in [29]. The work in [29] enables distributed MIMO operation as the local oscillation (LO) signal of the remote upconversion is synchronized with the CU. A 160.32 MHz bandwidth is presented in a $2 \times 1$ MISO configuration. However, this bandwidth is limited by the 10 Gbps data rate of the fiber connection and phase noise of the phase-locked loop (PLL) used [29]. In summary, there is a lack of flexible mm-wave RoF solutions suitable for MIMO applications.

In [30], we introduced an SDoF-based digital beamforming transmitter architecture based on commercial available hardware. Compared to the conference paper [30], this work extends the investigation of the proposed novel architecture significantly. A major extension is that link performance is now reported for up to 800 Msym/s, compared to 130 Msyms/s in [30]. The results of subchannel coherency, power level verification, and signal quality degradation of the RRH hardware is presented. Additionally, the over-the-air (OTA) experimental results reported in this work include, for example, a successful 500 Msym/s multiuser MIMO (MU-MIMO) wireless communication and 700 Msym/s MISO communication results. To the best of our knowledge, these symbol rate results represent the highest reported for mm-Wave SDoF MIMO applications.

This paper is structured as follows: Section II explains the transmitter architecture. Section III shows measurements and results. Finally, conclusions are drawn in Section IV.

## II. TRANSMITTER ARCHITECTURE

This section will start with introducing the hardware structure for the proposed transmitter architecture. Later, the channel estimation and precoding will be presented. This section ends with the baseband signal processing of the receiver (RX).

### A. Hardware Structure

The transmitter is based on a QSFP28 fiber connection between the CU and the RRH as in Fig. 3. The QSFP28 optical link includes four parallel high-speed digital channels at 25 Gbps each. The CU includes a PC (MATLAB) and a FPGA board. The PC generates baseband signals from initial random bits. The orthogonal pilots or precoded signals are four parallel baseband signals corresponding to the four mm-Wave channels in the RRH. A root-raised-cosine filter is used for pulse shaping to avoid intersymbol interference. The root-raised-cosine filter is configured with a 0.2 roll-off factor and four samples per symbol. The baseband signals need to be upsampled to 25 Gsps to match the data rate of the fiber link. Then, the baseband signals is numerically upconverted to an intermediate frequency (IF). The IF signals add an out-of-band sinusoidal signal to track the carrier frequency offset at the RX signal processing. The IF signals amplitude will be scaled to an optimum level of the following bandpass SDM (BPSDM) at 25 Gbps data rate [31]. The SDM order is 4 in this architecture implementation [32]. The signal processing mentioned above is done in the PC with offline signal processing. The FPGA board (Xilinx Virtex UltraScale+ HBM VCU128) is responsible for transmitting coherent BPSDM bitstreams through the fiber connection.

A commercial QSFP28 based optical fiber link connects the FPGA to the RRH as illustrated in Fig. 1. The QSFP28 transmits four parallel bitstreams to four parallel upconversion mixers (Analog Devices ADMV-1013) in the RRH. Each mixer can output mm-Wave frequencies between 24 GHz and 44 GHz. For single sideband upconversion, a 90° hybrid is used to feed the mixer with a quadrature IF signal. Ideally, a

bandpass filter is required to recover the analog IF signal from the SDM signal. However, in our system, the 90° hybrid and the mixer's IF input act as a bandpass filter, thus suppressing the majority of the out-of-band quantization noise. Moreover, the four parallel mixers are fed with the same LO signal to facilitate coherent upconversion of the IF signals. A signal synthesizer generates an LO signal originally, and the three power dividers promise coherent LO signals for the four mixers. The upconversion mixers include quadruplers, and accept LO frequencies in the range 5.4 GHz - 10.25 GHz. In our system, the 2.2 GHz IF signal is upconverted to 28 GHz center frequency according to $6.45$ GHz $\times 4 + 2.2$ GHz $= 28$ GHz. It is important to note that the center frequency can be controlled within the 24 GHz - 44 GHz range, either by changing the LO frequency or the IF frequency.

The TX antenna is simulated in CST Microwave Studio and designed for 28 GHz frequency. The TX antenna is a linear array patch antenna and can steer the transmitting beam in the azimuth direction. The antenna consists of 16 patch elements in total where each column of the antenna has four fixed patch elements which create a narrow elevation beam width. The separation distance between elements in azimuth/elevation direction is 5.35 mm/5.63 mm, respectively, corresponding to approximately a half wavelength at the center frequency. The half-power beamwidth of each column is 79.8°/20° in azimuth/elevation direction, respectively. The TX antenna has four independent feeding ports fed with the four parallel coherent signals from the RRH.

## B. Channel Estimation

The experiments are performed at a short distance in a stationary line-of-sight environment (as described in Section III). Hence, this work assumes a stable flat-fading channel.

In our experiments, the channel estimation is the first stage for digital beamforming and MU-MIMO. The CU generates pilot signals to the RRH and TX antenna at the channel estimation stage. An N-sample orthogonal pilot signal, $\mathbf{X}$, is generated by having one channel transmitting at a time:

$$\mathbf{X} = \begin{bmatrix} \mathbf{x}_0 & \mathbf{0} & \mathbf{0} & \mathbf{0} \\ \mathbf{0} & \mathbf{x}_1 & \mathbf{0} & \mathbf{0} \\ \mathbf{0} & \mathbf{0} & \mathbf{x}_2 & \mathbf{0} \\ \mathbf{0} & \mathbf{0} & \mathbf{0} & \mathbf{x}_3 \end{bmatrix}_{N \times 4}, \quad (1)$$

where $\mathbf{x}_0$, $\mathbf{x}_1$, $\mathbf{x}_2$, $\mathbf{x}_3$ are the four individual channel pilot sequences with uniform amplitude and random phases. These and $\mathbf{0}$, all have a dimension of $N/4 \times 1$.

The least-square channel estimation is given by:

$$\widehat{\mathbf{H}} = \begin{bmatrix} \widehat{h}_{10} & \widehat{h}_{11} & \widehat{h}_{12} & \widehat{h}_{13} \\ \widehat{h}_{20} & \widehat{h}_{21} & \widehat{h}_{22} & \widehat{h}_{23} \end{bmatrix}^{\mathrm{T}} = \left(\mathbf{X}^{\mathrm{T}}\mathbf{X}\right)^{-1}\mathbf{X}^{\mathrm{T}}\mathbf{Y}, \quad (2)$$

where $\mathbf{Y}$ is the received time aligned signal, with dimension $N \times 2$ for the two-user MU-MIMO case and dimension $N \times 1$ for the single-user MISO digital beamforming case. $\widehat{\mathbf{H}}$ is the estimated $4 \times 2$ channel matrix for MU-MIMO. The estimated channel vector has the dimension of $4 \times 1$ for digital beamforming MISO.
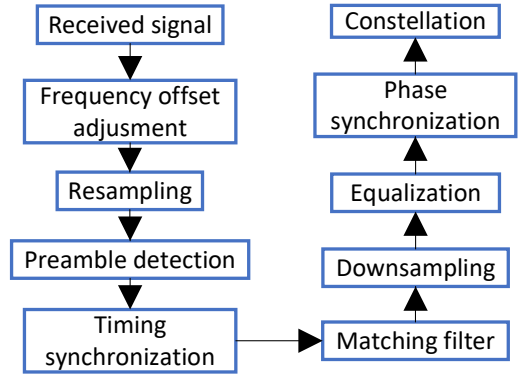


Fig. 2: The baseband signal processing steps at the receiver for MISO digital beamforming and MU-MIMO experiments.

## C. Precoding

In the MU-MIMO experiments, a zero-forcing (ZF) precoder has been used. The ZF precoder, $\mathbf{P}$, is defined as

$$\mathbf{P} = \left(\widehat{\mathbf{H}}\widehat{\mathbf{H}}^*\right)^{-1}\widehat{\mathbf{H}}. \quad (3)$$

To null interference at the receiver antennas, the ZF algorithm processes the user data, $\mathbf{U}$, to generate the MIMO signals, $\mathbf{S}$, as (4).

$$\mathbf{S} = \mathbf{U}\mathbf{P}^{\mathrm{T}}. \quad (4)$$

Since there is no inter-user interference in the digital beamforming MISO experiments, the four channels can radiate coherent signals with maximum output power. The precoder, $\mathbf{p}_{\mathrm{BF}}$, has been assigned uniform amplitude using the phase information from the ZF precoder, $\mathbf{P}$, as:

$$\mathbf{p}_{\mathrm{BF}} = \begin{bmatrix} e^{j\angle P_0} & e^{j\angle P_1} & e^{j\angle P_2} & e^{j\angle P_3} \end{bmatrix}^{\mathrm{T}} = e^{j\angle \mathbf{P}}. \quad (5)$$

The MISO beamforming precoder $\mathbf{p}_{\mathrm{BF}}$ processes user data according to (4) to generate the transmit signals.

## D. RX Baseband Signal Processing

For both the MISO and the MU-MIMO experiments, the system receiver requires signal processing steps to demodulate the user data. As shown in Fig. 2, the RX processing steps include frequency offset adjustment using the out-of-band sinusoidal signal, resampling to the matched filter sample rate, and detection of the preamble to synchronize the frames. Each frame needs timing synchronization, matched filtering, downsampling, equalization, and phase compensation for a final constellation [13].

## III. MEASUREMENTS AND RESULTS

The proposed architecture in Fig. 1 has been implemented and experimentally evaluated as presented in the diagram in Fig. 3 with two RX antennas (Antenna 1 and Antenna 2) corresponding to two users (User 1 and User 2). The RX
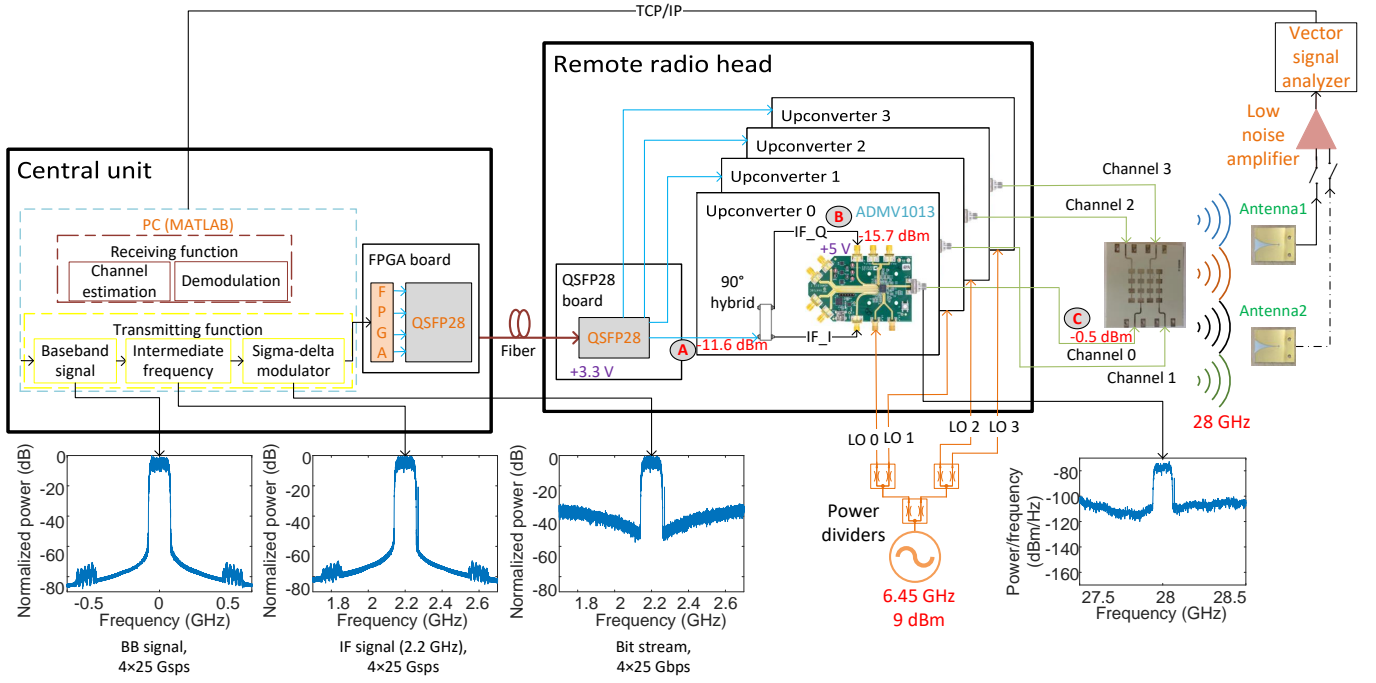
Fig. 3: Demonstration diagram of the proposed link architecture. Power levels and bandwidth performance are verified at positions A, B, and C of the remote radio head. There are the ideal signal spectrum of baseband signal, intermediate frequency signal and sigma-delta modulated signal with the mm-Wave measured spectrum. The transmitter introduces a sinusoidal signal next to the communication signal band for carrier frequency synchronization at the receiver. The two receiving antennas work as two users.

TABLE I: Commercial hardware list of the transmitter.

| Hardware | Manufacturer | Model | Quantity |
|---|---|---|---|
| FPGA board | Xilinx | VCU128 | 1 |
| QSFP28 | FS | QSFP28-SR4-100G | 2 |
| 90° Hybrid | Mini-Circuits | ZX10Q-2-27-S+ | 4 |
| Power divider | Mini-Circuits | ZX10R-14-S+ | 3 |
| Mixer | Analog Devices | EVAL-ADMV1013 | 4 |

TABLE II: Technical specifications of QSFP28 module.

| Specification | Description | Specification | Description |
|---|---|---|---|
| Wavelength | 850 nm | Connector | MTO[a]-12 |
| Media | Multi-mode fiber | Max fiber length | 100 m |
| TX Type | VCSEL[b] | Receiver Type | PIN[c] |
| TX Power | -8.4 to 2.4 dBm | Max Data Rate | 4x25.78 Gbps |

[a] Multifiber Termination Push-on/Pull-off.
[b] Vertical Cavity Surface Emitting Laser.
[c] Positive-Intrinsic-Negative photodiodes.

side also consists of one low noise amplifier (LNA) and one vector signal analyzer (VSA, Keysight N9042B). A photo of the experimental setup is shown in Fig. 4. The transmitter performance is first evaluated and then OTA experiments are performed to investigate the digital beamforming single-user MISO and MU-MIMO applications. In our measurements, the modulation scheme is single carrier 64 quadrature amplitude modulation (64-QAM).

In Table I, a list of the hardware used for the system has been reported. All of them are commercially available.

In Table II, some technical specifications of QSFP28 module used for the fiber connection are reported. QSFP28 module supports a maximum fiber length of 100 m, but the length in our implementation is limited to 10 m.

### A. Power Levels

The output power limits the wireless transmission distance. Therefore, we studied the power levels at different positions in the transmitter lineup, see positions labeled A/B/C in Fig. 3. The bandpower of the IF signal at position A is -11.6 dBm, and it is the same for all the QSFP28 output channels. At position B, the bandpower has dropped to -15.7 dBm, due to
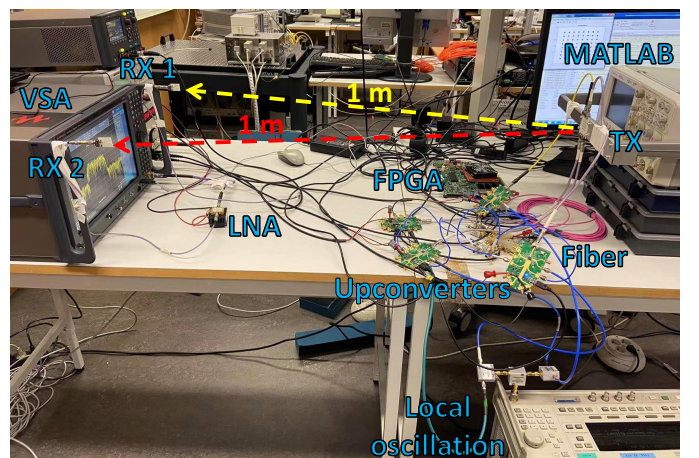


Fig. 4: The experimental setup used to demonstrate the proposed link architecture. The transmitting (TX) linear array antenna is placed at a 1 m distance from the receiving (RX) antennas. The two RX antennas are separated by 0.5 m.

the loss of 90° hybrid, SMA connector and coaxial cable. At position C, the active mixer has a 15.2 dB gain, resulting in -0.5 dBm inband output power for the mm-Wave signal. In fact, the mixer can provide up to 18 dB gain at the price of nonlinear impairments and then a severely degraded signal quality. It is worth noting that the power mentioned above is the average power. The peak power is 6.8 dB higher than the average power due to the 64-QAM signal's peak-to-average power ratio (PAPR).

Connecting the output of the mixer with the VSA at full span in spectrum analyzer mode, the output signal spectrum corresponds to Fig. 5a. The spectrum shows the inband signal with the quantization noise, the LO leakage and the lower sideband in the spectrum. The inband signal is at least 20 dB higher than the others. Fig. 5b shows the signal band power and the adjacent channel power ratio (ACPR), corresponding to - 0.5 dBm and 30.6 dBc, respectively. Fig. 5b has a sinusoidal peak at the right side of the signal spectrum for carrier frequency offset synchronization in RX signal processing, as described in Section II.A and II.D.
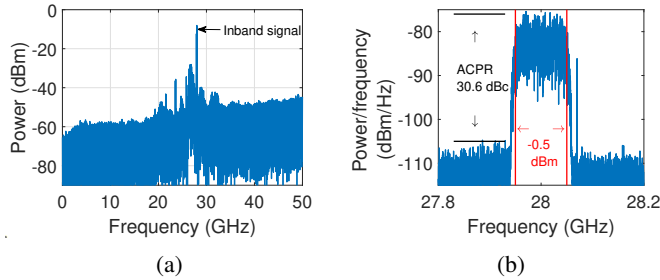


(a)　　　　(b)

Fig. 5: The output signal spectrum at position C of Fig. 3. (a) The inband signal is at least 20 dB higher than the quantization noise. (b) The signal band power and the adjacent channel power ratio (ACPR).

### B. Bandwidth Performance

In this section, we investigate how the performance of the transmitter depends on the symbol rate.

The normalized mean square error (NMSE) is used to estimate the signal quality. In Fig. 6, the bottom curve is the simulation (Sim) results and it has been reported as a benchmark for the measurements. With a fixed BPSDM sample rate of 25 Gsps, the less oversampling ratio (or the higher symbol rate) has the worse NMSE and the oversampling rate varies from 250 to 31.5 as the symbol rate changes from 100 MHz to 800 MHz. In general, all the NMSE curves in Fig. 6 match the trend of the simulated one. At 100 Msym/s symbol rate, the NMSE in position C is degraded compared to the ones at positions A and B. This slight difference is caused by the noise contributions from the mixer and VSA. At 700 Msym/s, the NMSE in positions A, B, and C is almost identical. Before position A, the hardware is compact in design and it is impossible to experimentally evaluate the signal quality from each stage. However, based on the observations in [13], the FPGA and optical transceivers both add noise contributions that degrade the signal quality from the ideal SDM coding to position A. At 800 Msym/s symbol rate, the NMSE in position C is slightly worse than at positions A
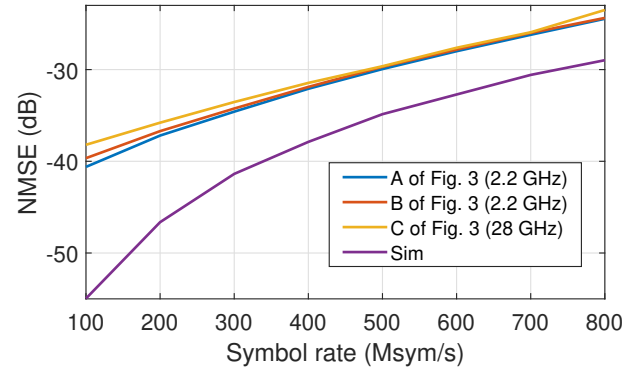


Fig. 6: Bandwidth performance analysis of the transmitter. The NMSE for an ideal sigma-delta modulated simulation is included as a reference (Sim). The NMSE results are measured at the positions A, B, and C in Fig. 3.

and B again, due to bandwidth limitation imposed by the 90° hybrid used. In conclusion, the RRH does not introduce critical performance degradation and this is in line with the observations made in [13]. At 800 Msym/s symbol rate, the ideal simulated performance is -28.9 dB, which is 5.4 dB better than the measurements. This shows that our measured performance is reasonably close to the simulation results, considering the inevitable hardware limitations present. For the symbol rate higher than 800 Msym/s, the system will be limited by 1 GHz bandwidth of the 90° hybrid.

### C. Fiber Link Coherence

Phase coherence is a crucial requirement in MIMO RoF systems [13] [14]. Link coherence has been evaluated according with the setup shown in Fig. 7. The CU generates four identical periodic bitstreams consisting of repeated eight ones and eight zeros to the fiber link. Due to the relationship between link data rate 25 Gbps and cyclic period, the frequency of the periodic bitstreams is 1.5625 GHz as in (6).

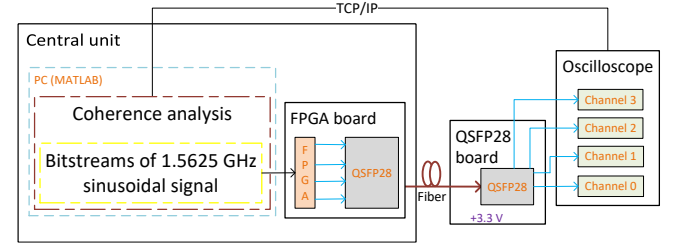$$f_{sin} = \frac{25 \text{ Gbps}}{8 + 8} = 1.5625 \text{ GHz}. \tag{6}$$



Fig. 7: The measurement setup used for fiber link coherence measurements. The central unit generates and transmits four identical sinusoidal signals to the four sub channels of QSFP28. The oscilloscope samples the four sinusoidal signals to determine their relative phase coherence.

The oscilloscope (RTO1044 Rohde & Schwarz) can sample the four sinusoidal signals from the QSFP28 at 10 Gsps, simultaneously. The coherence analysis numerically downconverts the oscilloscope samples by the sinusoidal frequency and

extracts the amplitude and phase from the samples. Fig. 8 reports the coherence of the four 1.5625 GHz sinusoidal signals by considering 1,000,000 oscilloscope samples. Firstly, in Fig. 8a, we normalized the phase and amplitude of the channel between the receiver and Channel 3. From the figure, we can conclude that the amplitude and phase difference between the channels is very stable. The amplitude difference is less than 0.3 dB between the channels. In theory, the four fiber sub-channels are supposed to have a similar phase because the fiber connection is only 10 m in length. However, there is a phase difference of around 150° between channels 1&2 and 0&3. The phase difference in the measurements results from a small difference in the length of the coaxial cable connections between QSFP28 PCB board and the oscilloscope channels. During measurements, we were not able to find four identical cables and all of them have slightly different lengths. Secondly, the phase difference in the measurement results is from our customized QSFP28 PCB board, where the four transmission lines have different electrical lengths.
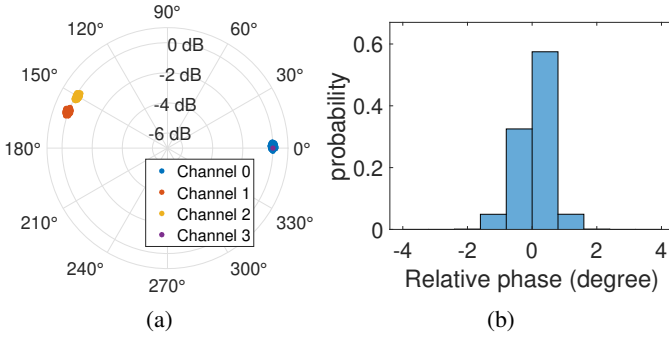


Fig. 8: The fiber link coherence of four channels of the QSFP28. (a) Polar plot of link coherence for the four channels, normalized to the phase and amplitude of Channel 3. (b) Histogram of the normalized phase difference of all channels.

In order to summarize the overall phase coherency between the channels, we further normalized each channel's phase information with the corresponding mean phase to summarize all phase variations in the same histogram plot. Fig. 8b shows that the phase difference within -2° to 2° centralized at 0°, and the standard deviation of the phase difference is only 1.2°. In conclusion, the results show that the proposed architecture can provide a very stable and coherent transmission of four channels from the CU to the RRH. In the next subsections, we use this as a foundation for digital beamforming MISO and MU-MIMO OTA transmission experiments.

The connection between CU QSFP28 and RRH QSFP28 is a 10 m long cable with multifiber termination push-on (MTO-12) connectors at two ends. The cable includes twelve fibers, four of which are used to transmit four data streams in this implementation. They will have a constant slight phase difference for the optical signal. During the following OTA measurements, we are accounting for the total phase differences of the system by channel estimation and compensating for this phase difference by precoding.

## D. SISO and MISO Measurements

The RX antennas are separated by a distance of 1.0 m with TX linear array antenna, as shown in Fig. 4. Channel 3 (TX) and RX User 1 have been used for SISO OTA measurement. For digital beamforming MISO measurements, there are two steps of channel estimation and digital beamforming. In the channel estimation step, we connect User 1 with LNA while four channels of the RRH radiate pilot signals (1) using the TX linear array antenna. In the digital beamforming step, we perform the MISO measurement by precoding as described in Section II.C.

Digital beamforming helps to compensate for the propagation loss and it is dependent on estimated channel information, as illustrated in Section II. Hence, channel information stability is essential. The polar plot in Fig. 9a presents the channel coefficients from 208 repeated OTA measurements, normalized to the phase and amplitude of the channel between User 1 and Channel 3. The normalized {amplitude, phase} channel information is $\{-0.69 \text{ dB}, -150°\} / \{-0.69 \text{ dB}, 45°\} / \{-1.04 \text{ dB}, 142°\}$ for the remaining channels Channel 0/Channel 1/Channel 2, respectively. The amplitude difference between the four channels is only 1 dB, which can be explained by the fact that the four elements of the TX antenna are mounted at the same height as the RX User 1. We further normalized each channel's phase information with the corresponding mean phase to summarize all phase variations in Fig. 9b, which presents the phase variations of all channel coefficients. Almost 62% of the phase variation is between -1° and 1° with a maximum phase variation remaining within -2° to 2°. In conclusion, this MISO demonstration promises precise system stability.
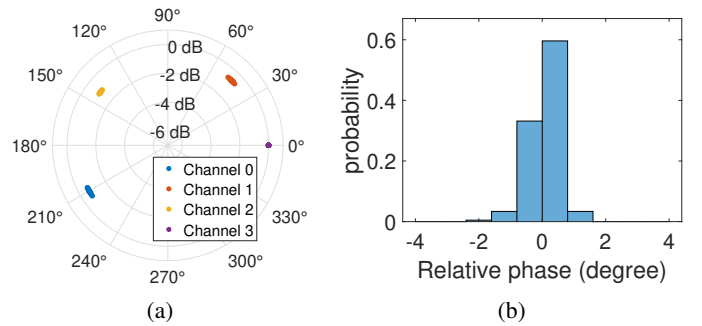


Fig. 9: The channel estimation results from 208 repeated digital beamforming over-the-air MISO measurements. (a) Polar plot of channel information for the four channels. (b) Histogram of normalized phase variations obtained from the channel information.

In Fig. 10, there are SISO and MISO OTA measurement results comparing the ideal simulation results (Sim) of BPSDM and the TX performance (position C of Fig. 3). Due to the propagation loss at 1 m distance, SISO OTA is noise limited and therefore has the worst NMSE in Fig. 10. With all the TX channels active (MISO), and applying the digital beamforming precoding from (5) and (4), the NMSE is improved and becomes close to the performance of the TX in position C.
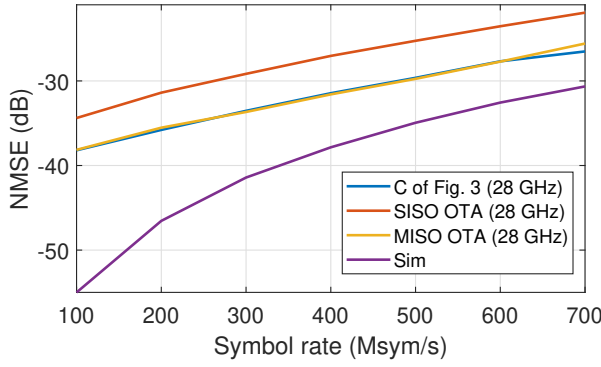
Fig. 10: Bandwidth performance analysis of over-the-air (OTA) measurements. The NMSE for an ideal simulation result (Sim) of sigma-delta modulation is included as a reference. One channel over-the-air measurement (SISO OTA (28 GHz)) is comparing with cabled connected measurement (C of Fig .1 (28 GHz)) and OTA beamforming measurements (MISO OTA (28 GHz)).

In Fig. 11a, the received inband power of SISO OTA measurement is -8.1 dBm, while Fig. 11c shows that the inband power has increased to 3.2 dBm when the MISO digital beamforming is activated. It means that the MISO digital beamforming improves the received signal power by 11.3 dB. Which is consistent with a four-channel beamforming corresponding to a 12 dB (16 times) equivalent isotropically radiated power (EIRP) increment. Accounting for channel amplitude differences in reality, the power results in the measurements agree well with the theoretical prediction. The peak at the right of the inband power is used to track the frequency offset during the demonstration, as described in Section II.A and II.D.

When the MISO received inband power is 11.3 dB higher than the SISO OTA inband power, the NMSE is only improved by 5 dB. The MISO digital beamforming NMSE is limited by the RRH performances since the yellow curve is close to the blue curve in Fig. 10. The $6.3$ dB $= 11.3$ dB $- 5$ dB power gain can be used to reach a 2 m OTA distance (double distance) without a significant performance degradation at 700 Msym/s (4.2 Gbit/s with 64QAM).

### E. MU-MIMO Measurements

In MU-MIMO, both RX antennas (users) are activated. They have a separation of 0.5 m and represent two spatially separated users served by the same TX linear array antenna. The TX linear array antenna is placed at a distance of 1 m from the RX antennas. By manually switching between the two antennas, the use of a single LNA and VSA is permitted: in the channel estimation step, after uploaded pilot signals to RRH, we first connect User 1 with LNA, then connect User 2. To generate the polar plots of Fig. 12a/b, the estimated channel information is normalized to the channel between channel 3 and User 1/User 2. In Fig. 12c/d, each channel's phase information is normalized with the corresponding mean phase, so that the histograms show the phase variations around 0°. The results from the channel estimation of User 1 are presented in Fig. 12a/c, while the channel information of User 2 is presented in Fig. 12b/d. The histograms of phase variations are always between -2° and 2°. It means that the channel estimation is stable for MU-MIMO measurements.
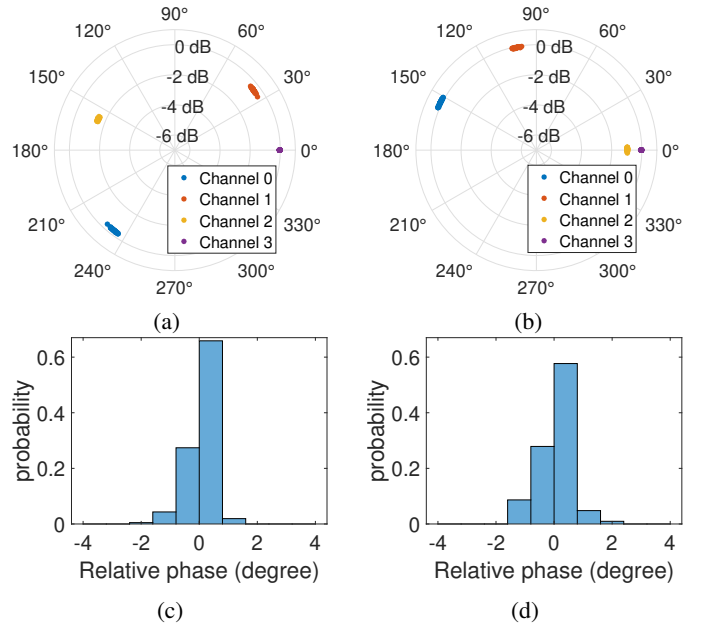


Fig. 12: The channel estimation results from 225 repeated MU-MIMO over-the-air measurements. (a) Polar plot of channel information between transmitter and User 1. (b) Polar plot of channel information between transmitter and User 2. (c) Histogram of normalized channel phase variations for User 1. (d) Histogram of normalized channel phase variations for User 2.
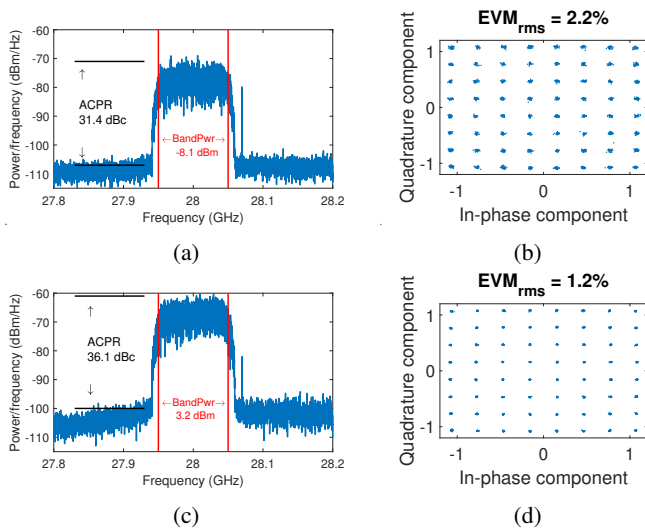


Fig. 11: The received band power (BandPwr), the adjacent channel power ratio (ACPR), and the error vector magnitude (EVM) at the receiver. The peak at the right of the band power is used to track the frequency offset during the demonstration. (a) SISO over-the-air measurement. (b) SISO over-the-air constellation. (c) Digital beamforming MISO over-the-air measurement. (d) Digital beamforming MISO over-the-air constellation.

TABLE III: Comparison with the state-of-the-art RoF publications.

| Ref. | RoF | MIMO | Symbol rate | Modulation | OTA distance | Carrier frequency | NMSE |
|------|-----|------|-------------|------------|--------------|-------------------|------|
| [20] | ARoF | $1 \times 1$ | 1.96 Gsym/s | 16-QAM OFDM | 2.2 m | 28 GHz | -14 dB[a] |
| [33] | ARoF | $2 \times 2$ | 1 Gsym/s | 64-QAM OFDM | 10 m | 28 GHz | -24.3 dB |
| [23] | ARoF | $9 \times 1$ | 100 Msym/s | 64-QAM OFDM | 6.3 m | 28 GHz | -31.3 dB |
| [25] | ARoF | $2 \times 2$[b] | 22 Gsym/s | 16-QAM | 0.2 m | 140 GHz | -14 dB[a] |
| [26] | ARoF | $2 \times 1$ | 3 Gsym/s | 64-QAM | 1.5 m | 28 GHz | -23 dB |
| [34] | ARoF | $8 \times 1$ | 3.5 Gsym/s | 16-QAM | 0.5 m | 60 GHz | -19.6 dB |
| [35] | SDoF | $2 \times 1$ | 160.32 Msym/s | 64-QAM OFDM | 2.0 m | > 24 GHz | -24.4 dB |
| This work | SDoF | $4 \times 1$ | 700 Msym/s | 64-QAM | 1.0 m | 28 GHz | -25.2 dB |
| This work | SDoF | $4 \times 2$ | 500 Msym/s | 64-QAM | 1.0 m | 28 GHz | -22 dB |

[a] The paper reached the bit-error-rate (BER) limit corresponding to forward error corrections (FEC) with 25% overhead. The NMSE requirement for this BER limit is 14 dB.
[b] This is only antenna configuration and does not have MIMO precoding.
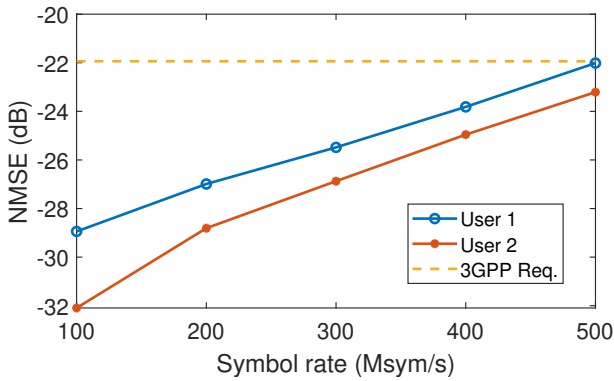


Fig. 13: NMSE results of MU-MIMO measurements. The NMSE results of two users satisfy the 3GPP requirement (dashed line).

At the ZF precoding evaluation step, the CU generates ZF MU-MIMO data to the RRH, according to (3) and (4). The receiver performs baseband signal demodulation for the signal received by User 2, since User 2 is already connected with LNA and VSA from the previous channel estimation step. By switching User 1 to LNA again, the receiver does baseband signal demodulation for the signal received by User 1. Repeating these procedures above, the symbol rate varies from 100 Msym/s to 500 Msym/s. The MU-MIMO NMSE results are presented in Fig. 13. Both users of User 1 and User 2 can satisfy the NMSE requirements of the 3GPP specifications [36] for 64-QAM signal.

User 2 shows better NMSE than User 1, and the NMSE results do not change even if we change the switching order during measurements. This means that the limitation is probably due to the position and radiation of RX/TX antennas causing a difference in the effective signal power received [37]. With a greater symbol rate, the NMSE becomes worse. Firstly, the worse NMSE is due to the bandwidth performance of the RRH, as studied in section III.B. Secondly, this demonstration only includes one tap for each channel in the channel estimation, which may be insufficient to represent the channel frequency response for large bandwidths. Therefore, we will study better channel estimation and precoding algorithms for MIMO applications in our future work.

We have also studied inter-user interference of the MU-MIMO measurements by comparing the error spectrum with the received spectrum. The error spectrum is a frequency domain representation of the difference between the demodulated constellation and the reference constellation for users. As the spectrums in Fig. 14 show, the error spectrum is higher than the out-of-band noise level of the received signal and has a distinct frequency response. This can not be explained by residual linear distortion of the received signal since a powerful 40 taps equalizer had been applied. Nonlinear distortion can also be excluded since there is no sign of out-of-band distortion sidebands. Finally, residual phase noise is also not visible in the demodulated constellation.

This means that the inband distortion is caused by inter-user interference in the MU-MIMO transmission case. For 100 Msym/s, users have -28.9 dB/-32.1 dB inter-user interference which dominates the overall NMSE in MU-MIMO transmission, as shown in Fig. 14a/b.
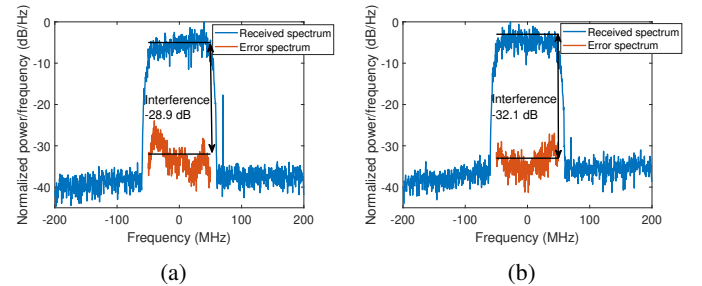


Fig. 14: Interference of the over-the-air MU-MIMO measurements at 100 Msym/s. (a) User 1's interference; (b) User 2's interference.

## IV. Conclusion

This paper proposes a mm-Wave SDoF transmitter implemented with commercially available hardware. Digital beamforming MISO and MU-MIMO functionalities are evaluated at a 1 m wireless distance with the transmitter. The digital beamforming MISO measurement demonstrates a mm-Wave, 28 GHz, transmission of a 700 Msym/s 64QAM signal with -25.2 dB NMSE by improving the inband power by 11.3 dB

compared to a single channel transmission. The MU-MIMO demonstrates the serving of two simultaneous users with a 500 Msym/s rate with a NMSE of -22 dB, which complies with the 3GPP requirements.

It has been proven that the transmitter is very stable, making it well suited for high-performance MIMO experiments. The comparison with the state-of-the-art RoF publications reported in Table III concludes that this work is the first mm-Wave SDoF solution supporting multiple users. This demonstration can form the basis for the mm-Wave active distributed antenna system with stable coherence.

## REFERENCES

[1] J. Navarro-Ortiz, P. Romero-Diaz, S. Sendra, P. Ameigeiras, J. J. Ramos-Munoz, and J. M. Lopez-Soler, "A Survey on 5G Usage Scenarios and Traffic Models," *IEEE Communications Surveys Tutorials*, vol. 22, no. 2, pp. 905–929, Secondquarter 2020.

[2] M. Jaber, M. A. Imran, R. Tafazolli, and A. Tukmanov, "5G Backhaul Challenges and Emerging Research Directions: A Survey," *IEEE Access*, vol. 4, pp. 1743–1766, 2016.

[3] J. M. Khurpade, D. Rao, and P. D. Sanghavi, "A Survey on IOT and 5G Network," *2018 International Conference on Smart City and Emerging Technology (ICSCET)*, pp. 1–3, Jan 2018.

[4] J. G. Andrews, S. Buzzi, W. Choi, S. V. Hanly, A. Lozano, A. C. Soong, and J. C. Zhang, "What Will 5G Be?" *IEEE Journal on selected areas in communications*, vol. 32, no. 6, pp. 1065–1082, 2014.

[5] W. Feng, Y. Wang, D. Lin, N. Ge, J. Lu, and S. Li, "When mmWave Communications Meet Network Densification: A Scalable Interference Coordination Perspective," *IEEE Journal on Selected Areas in Communications*, vol. 35, no. 7, pp. 1459–1471, 2017.

[6] E. Rådahl and S. Rimborg, "Simulations of the Capacity and Coverage for a Multi-User Distributed MIMO Network," *Chalmers Open Digital Repository*, 2021.

[7] A. Shaikh and M. J. Kaur, "Comprehensive Survey of Massive MIMO for 5G Communications," in *2019 Advances in Science and Engineering Technology International Conferences (ASET)*, March 2019, pp. 1–5.

[8] P. P. Monteiro, A. Gameiro, and N. J. Gomes, *Next Generation Wireless Communications Using Radio over Fiber*. John Wiley & Sons, 2012.

[9] A. Gupta and R. K. Jha, "A Survey of 5G Network: Architecture and Emerging Technologies," *IEEE Access*, vol. 3, pp. 1206–1232, 2015.

[10] K. Zhu, M. J. Crisp, S. He, R. V. Penty, and I. H. White, "MIMO System Capacity Improvements Using Radio-over-Fibre Distributed Antenna System Technology," in *2011 Optical Fiber Communication Conference and Exposition and the National Fiber Optic Engineers Conference*, March 2011, pp. 1–3.

[11] P. Pesek, J. Bohata, S. Zvanovec, and J. Perez, "Characterization of dual-polarization analogue radio over fiber fronthaul for LTE C-RAN architecture," in *2016 10th International Symposium on Communication Systems, Networks and Digital Signal Processing (CSNDSP)*, 2016, pp. 1–4.

[12] Y. Yang, C. Lim, and A. Nirmalathas, "Experimental demonstration of a downlink multi-channel Hybrid Fiber-Radio using digitized RF-over-fiber technique," in *2010 IEEE MTT-S International Microwave Symposium*, May 2010, pp. 748–751.

[13] I. C. Sezgin, M. Dahlgren, T. Eriksson, M. Coldrey, C. Larsson, J. Gustavsson, and C. Fager, "A Low-Complexity Distributed-MIMO Testbed Based on High-Speed Sigma–Delta-Over-Fiber," *IEEE Transactions on Microwave Theory and Techniques*, vol. 67, no. 7, pp. 2861–2872, July 2019.

[14] C.-Y. Wu, H. Li, O. Caytan, J. Van Kerrebrouck, L. Breyne, J. Bauwelinck, P. Demeester, and G. Torfs, "Distributed Multi-User MIMO Transmission Using Real-Time Sigma-Delta-Over-Fiber for Next Generation Fronthaul Interface," *Journal of Lightwave Technology*, vol. 38, no. 4, pp. 705–713, Feb 2020.

[15] Y. Li, F. Wang, M. El-Hajjar, and L. Hanzo, "Analog Radio-over-Fiber-Aided Optical-Domain MIMO Signal Processing for High-Performance Low-Cost Radio Access Networks," *IEEE Communications Magazine*, vol. 59, no. 1, January 2021.

[16] L. Breyne, G. Torfs, X. Yin, P. Demeester, and J. Bauwelinck, "Comparison Between Analog Radio-Over-Fiber and Sigma Delta Modulated Radio-Over-Fiber," *IEEE Photonics Technology Letters*, vol. 29, no. 21, pp. 1808–1811, 2017.

[17] F. Olofsson, L. Aabel, M. Karlsson, and C. Fager, "Comparison of Transmitter Nonlinearity Impairments in externally modulated Sigma-Delta-over Fiber vs Analog Radio-over-Fiber links," in *2022 Optical Fiber Communications Conference and Exhibition (OFC)*. IEEE, 2022, pp. 1–3.

[18] A. H. M. R. Islam, M. Bakaul, and A. Nirmalathas, "Multilevel Modulations for Gigabit Access in a Simple Millimeter-Wave Radio-Over-Fiber Link," *IEEE Photonics Technology Letters*, vol. 24, no. 20, pp. 1860–1863, Oct 2012.

[19] D. Perez-Galacho, D. Sartiano, and S. Sales, "Analog Radio over Fiber Links for Future 5G Radio Access Networks," in *2019 21st International Conference on Transparent Optical Networks (ICTON)*, July 2019, pp. 1–4.

[20] D. Konstantinou, T. A. Bressner, S. Rommel, U. Johannsen, M. N. Johansson, M. V. Ivashina, A. B. Smolders, and I. T. Monroy, "5G RAN architecture based on analog radio-over-fiber fronthaul over UDWDM-PON and phased array fed reflector antennas," *Optics Communications*, vol. 454, p. 124464, 2020.

[21] L. Bogaert, J. Van Kerrebrouck, H. Li, I. L. de Paula, K. Van Gasse, C.-Y. Wu, P. Ossieur, S. Lemey, H. Rogier, P. Demeester, G. Roelkens, J. Bauwelinck, and G. Torfs, "SiPhotonics/GaAs 28-GHz Transceiver With Reflective EAM for Laser-Less mmWave-Over-Fiber," *Journal of Lightwave Technology*, vol. 39, no. 3, pp. 779–786, Feb 2021.

[22] R. X. F. Budé, M. M. A. Versluis, G. I. Nazarikov, S. Rommel, B. G. M. van Ark, U. Johannsen, I. T. Monroy, and A. B. Smolders, "Millimeter-Wave Outphasing using Analog-Radio over Fiber for 5G Physical Layer Infrastructure," in *2020 50th European Microwave Conference (EuMC)*, Jan 2021, pp. 288–291.

[23] K. Ito, M. Suga, T. Arai, Y. Shirato, N. Kita, and T. Onizawa, "Passive beamformer based remote beamforming scheme for radio-over-fiber systems: Experimental demonstration using 28-GHz band reflectarray," *Optics Communications*, vol. 513, p. 128026, 2022.

[24] I. L. de Paula, L. Bogaert, O. Caytan *et al.*, "Air-Filled SIW Remote Antenna Unit with True Time Delay Optical Beamforming for mmWave-over-Fiber Systems," *Journal of Lightwave Technology*, pp. 1–15, 2022.

[25] R. Puerta, J. Yu, X. Li, Y. Xu, J. J. Vegas Olmos, and I. Tafur Monroy, "Single-Carrier Dual-Polarization 328-Gb/s Wireless Transmission in a D-Band Millimeter Wave 2 × 2 MU-MIMO Radio-Over-Fiber System," *Journal of Lightwave Technology*, vol. 36, no. 2, pp. 587–593, 2018.

[26] A. Moerman, J. Van Kerrebrouck, O. Caytan, I. L. de Paula, L. Bogaert, G. Torfs, P. Demeester, M. Moeneclaey, H. Rogier, and S. Lemey, "mmWave-over-Fiber Distributed Antenna Systems for Reliable multi-Gbps Wireless Communication," in *2022 3rd URSI Atlantic and Asia Pacific Radio Science Meeting (AT-AP-RASC)*, May 2022, pp. 1–4.

[27] M. Sung, J. Kim, E.-S. Kim, S.-H. Cho, Y.-J. Won, B.-C. Lim, S.-Y. Pyun, J. K. Lee, and J. H. Lee, "Demonstration of 5G Trial Service in 28 GHz Millimeter Wave using IFoF-Based Analog Distributed Antenna System," in *2019 Optical Fiber Communications Conference and Exhibition (OFC)*, March 2019, pp. 1–3.

[28] H. Li, M. Verplaetse, J. Verbist, J. Van Kerrebrouck, L. Breyne, C.-Y. Wu, L. Bogaert, B. Moeneclaey, X. Yin, J. Bauwelinck, P. Demeester, and G. Torfs, "Real-Time 100-GS/s Sigma-Delta Modulator for All-Digital Radio-Over-Fiber Transmission," *Journal of Lightwave Technology*, vol. 38, no. 2, pp. 386–393, 2020.

[29] C.-Y. Wu, H. Li, J. Van Kerrebrouck, A. Vandierendonck, I. L. de Paula, L. Breyne, O. Caytan, S. Lemey, H. Rogier, J. Bauwelinck, P. Demeester, and G. Torfs, "Distributed Antenna System Using Sigma-Delta Intermediate-Frequency-Over-Fiber for Frequency Bands Above 24 GHz," *Journal of Lightwave Technology*, vol. 38, no. 10, pp. 2765–2773, May 2020.

[30] H. Bao, Z. S. He, F. Ponzini, and C. Fager, "Demonstration of Flexible mmWave Digital Beamforming Transmitter using Sigma-Delta Radio-Over-Fiber Link," in *2022 52nd European Microwave Conference (EuMC)*, 2022, pp. 692–695.

[31] R. Schreier, G. C. Temes *et al.*, *Understanding Delta-Sigma Data Converters*. Piscataway, NJ: IEEE press, 2005, vol. 74.

[32] R. Schreier, "Delta Sigma Toolbox," Accessed: 2022-12-12. [Online]. Available: https://www.mathworks.com/matlabcentral/fileexchange/19-delta-sigma-toolbox

[33] M. Sung, J. Kim, E.-S. Kim, S.-H. Cho, Y.-J. Won, B.-C. Lim, S.-Y. Pyun, H. Lee, J. K. Lee, and J. H. Lee, "RoF-Based Radio Access Network for 5G Mobile Communication Systems in 28 GHz Millimeter-Wave," *Journal of Lightwave Technology*, vol. 38, no. 2, pp. 409–420, 2020.

[34] T. Nagayama, S. Akiba, T. Tomura, and J. Hirokawa, "Photonics-Based Millimeter-Wave Band Remote Beamforming of Array-Antenna Integrated With Photodiode Using Variable Optical Delay Line and Attenuator," *Journal of Lightwave Technology*, vol. 36, no. 19, pp. 4416–4422, 2018.

[35] C.-Y. Wu, H. Li, J. Van Kerrebrouck, A. Vandierendonck, I. L. de Paula, L. Breyne, O. Caytan, S. Lemey, H. Rogier, J. Bauwelinck *et al.*, "Distributed Antenna System Using Sigma-Delta Intermediate-Frequency-Over-Fiber for Frequency Bands Above 24 GHz," *Journal of Lightwave Technology*, vol. 38, no. 10, pp. 2765–2773, 2020.

[36] *Evolved Universal Terrestrial Radio Access (E-UTRA); Base Station (BS) radio transmission and reception (release 16) (V16.3.0)*, 3GPP, 2019, tS 36.104.

[37] T. Ingason and H. Liu, "Line-of-Sight MIMO for Microwave Links-Adaptive Dual Polarized and Spatially Separated Systems," Master's thesis, Chalmers University of Technology, 2009.

**Husileng Bao** (Student Member, IEEE) received the M.Sc. degree in electronics and communication engineering from the Beijing Institute of Technology, Beijing, China, in 2016. He worked as an engineer for Tsinghua University, Beijing, China until 2018. Then he joined Ericsson, Beijing, China. Since 2020, he has been working toward the Ph.D. degree as a Marie Curie early-stage-researcher with the Microwave Electronics Laboratory, Department of Microtechnology and Nanoscience (MC2), Chalmers University of Technology, Gothenburg, Sweden. His main research interests include MIMO communication and radio-over-fiber.



**Filippo Ponzini** Filippo Ponzini was born in Piacenza, Italy, in 1973. He received the master's degree in telecommunications engineering from the University of Parma, Italy. He was a Researcher in optical technologies with the Scuola Superiore Sant'Anna, Pisa, Italy. Since 2007, he has been with Ericsson Research. He is currently involved in optical datacenters architectures and optical networks and systems for 5G radio access networks. He has authored over 30 publications and international patents.



**Christian Fager** (Senior Member, IEEE) received the Ph.D. degree from the Chalmers University of Technology, Gothenburg, Sweden, in 2003. He is currently a Full Professor with the Chalmers University of Technology and Head of the Microwave Electronics Laboratory. He has authored or coauthored more than 140 publications in international journals and conferences. His current research interest includes energy efficient and linear transmitters for future wireless communication systems. He is an Associate Editor for IEEE Microwave Magazine and IEEE Microwave and Wireless Components Letters. He is a Representative for Sweden, Norway, and Iceland in the European Microwave Association (EuMA). He is a TPC Member of the IEEE MTT-S International Microwave Symposium and is also the Chair or Co-Chair of the 2020 or 2021 IEEE Topical Conference on RF/microwave Power Amplifiers, and TPC Co-Chair for the 2020 European Microwave Integrated Circuits Conference. He was the recipient of the Chalmers Supervisor of the Year Award in 2018 and the IEEE International Microwave Symposium Best Student Paper Award in 2002.